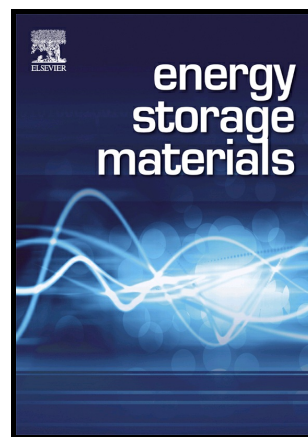


## Author's Accepted Manuscript

Phosphorous-Containing Oxygen-Deficient Cobalt Molybdate as an Advanced Electrode Material for Supercapacitors

Shude Liu, Ying Yin, Dixing Ni, Kwan San Hui, Kwun Nam Hui, Chu-Ying Ouyang, Seong Chan Jun



PII: S2405-8297(18)30843-2  
DOI: <https://doi.org/10.1016/j.ensm.2018.10.022>  
Reference: ENSM544

To appear in: *Energy Storage Materials*

Received date: 8 July 2018  
Revised date: 17 October 2018  
Accepted date: 27 October 2018

Cite this article as: Shude Liu, Ying Yin, Dixing Ni, Kwan San Hui, Kwun Nam Hui, Chu-Ying Ouyang and Seong Chan Jun, Phosphorous-Containing Oxygen-Deficient Cobalt Molybdate as an Advanced Electrode Material for Supercapacitors, *Energy Storage Materials*, <https://doi.org/10.1016/j.ensm.2018.10.022>

This is a PDF file of an unedited manuscript that has been accepted for publication. As a service to our customers we are providing this early version of the manuscript. The manuscript will undergo copyediting, typesetting, and review of the resulting galley proof before it is published in its final citable form. Please note that during the production process errors may be discovered which could affect the content, and all legal disclaimers that apply to the journal pertain.

## Phosphorous-Containing Oxygen-Deficient Cobalt Molybdate as an Advanced Electrode Material for Supercapacitors

Shude Liu<sup>1</sup>, YingYin<sup>1,2</sup>, Dixing Ni<sup>3</sup>, Kwan San Hui<sup>4</sup>, Kwun Nam Hui<sup>\*5</sup>, Chu-Ying Ouyang<sup>\*3</sup>, Seong Chan Jun<sup>\*1</sup>

<sup>1</sup>School of Mechanical Engineering, Yonsei University, Seoul 120-749, South Korea.

<sup>2</sup>Guangxi Key Laboratory of Information Materials, Guilin University of Electronic Technology, Guilin 541004, PR China.

<sup>3</sup>Department of Physics, Jiangxi Normal University, Nanchang, 330022, China.

<sup>4</sup>School of Mathematics, University of East Anglia, Norwich, NR4 7TJ, United Kingdom.

<sup>5</sup>Joint Key Laboratory of the Ministry of Education, Institute of Applied Physics and Materials Engineering, University of Macau, Avenida da Universidade, Taipa, Macau, China.

bizhui@umac.mo

cyouyang@hotmail.com

scj@yonsei.ac.kr

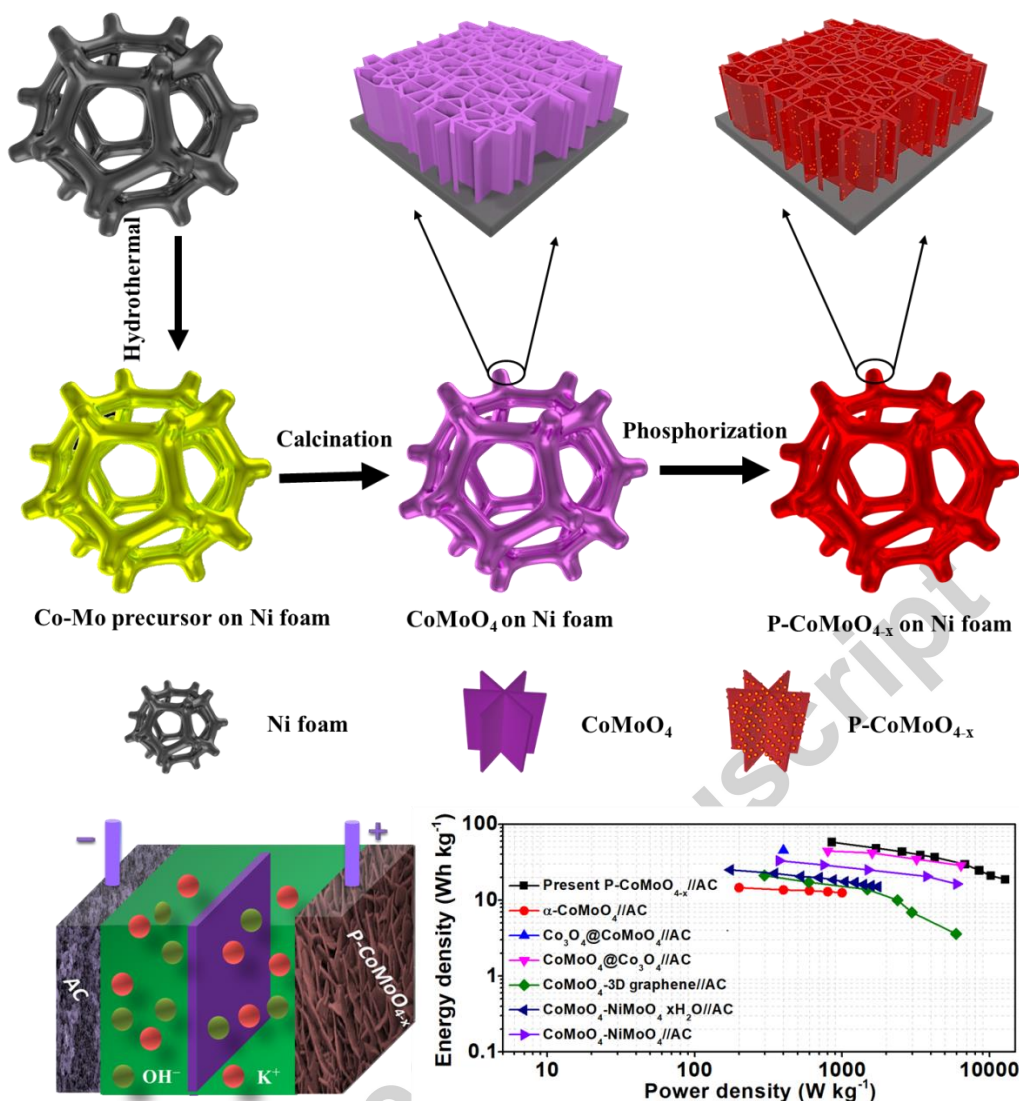
\*Corresponding author's:

### Abstract

The intrinsically poor electrical conductivity and insufficient number of electrochemically active sites of transition-metal oxides hamper their wide application in high-performance supercapacitors. Herein, we demonstrate an effective strategy of creating phosphorus-containing cobalt molybdate ( $\text{CoMoO}_4$ ) with oxygen vacancies ( $\text{P-CoMoO}_{4-x}$ ) on nickel foam for use as a supercapacitor electrode. Experimental

analyses and theoretical calculations reveal that the electronic structure of P-CoMoO<sub>4-x</sub> can be efficiently modulated by incorporating P heteroatoms and O vacancies, thereby simultaneously reducing the energy band gap and increasing electrical conductivity. Moreover, incorporating P into P-CoMoO<sub>4-x</sub> weakens the Co-O bond energy and induces the low oxidation states of molybdenum species, facilitating surface redox chemistry and improving electrochemical performance. Accordingly, the optimized P-CoMoO<sub>4-x</sub> electrode exhibits a high specific capacity of 1368 C g<sup>-1</sup> at a current density of 2 A g<sup>-1</sup>, and it retains 95.3% of the initial capacity after 5000 cycles at a high current density of 10 A g<sup>-1</sup>. An asymmetric supercapacitor assembled with the optimized P-CoMoO<sub>4-x</sub> as positive electrode and activated carbon as negative electrode delivers a high energy density of 58 W h kg<sup>-1</sup> at a power density of 850 W kg<sup>-1</sup> as well as achieves excellent cycling lifespan.

### Graphical Abstract



We have demonstrated a facile strategy for creating O vacancies and incorporating P atoms in P-CoMoO<sub>4-x</sub> nanosheets on conductive Ni foam. Experimental and theoretical studies provide insight into the effect of the introduction of P and of O vacancies on structural and electrical properties of P-CoMoO<sub>4-x</sub>. Moreover, P incorporation into the P-CoMoO<sub>4-x</sub> lattice induces reduction in bond energy of Co-O and the formation of Mo species with a lower oxidation state, resulting in substantially enhanced redox reaction kinetics and electrochemical performance.

Accordingly, the optimized P-CoMoO<sub>4-x</sub> achieves a high specific capacity of 1368 C g<sup>-1</sup> at a current density of 2 A g<sup>-1</sup>, and excellent electrochemical stability. The asymmetric supercapacitor P-CoMoO<sub>4-x</sub>//AC delivers superior energy densities of 58 W h kg<sup>-1</sup> at a power density of 850 W kg<sup>-1</sup>.

**Keywords:**

CoMoO<sub>4</sub>, phosphorus incorporation, oxygen vacancy, electrochemical performance, supercapacitors

**1. Introduction**

Supercapacitors are one of the most efficient classes of electrochemical storage devices because of their higher power density, faster charge–discharge rate, and longer lifespan than those of lithium-ion batteries [1, 2]. With regard to the charge storage mechanism of electrode materials, conventional carbonaceous materials store electrical energy through electrostatic accumulation of surface charge [3, 4], whereas transition-metal oxides involve fast reversible Faradaic reactions at the surface or at a near-surface region, producing higher energy densities [5, 6]. However, the high energy density of transition-metal oxides is achieved by sacrificing power density and cycling lifetime, impeding their large-scale practical application in supercapacitors [7, 8]. The demand for supercapacitors with favorable energy and power densities has stimulated tremendous research interest on the exploration of novel nanostructured electrode materials.

Among transition metal oxides, multiple metal oxides have been widely investigated as promising alternatives for supercapacitors because of their accessible oxidation states, higher reversible capacities, and better electrical conductivity than unitary metal oxides [9-11]. Recently, cobalt molybdate ( $\text{CoMoO}_4$ ) is attracting ever-growing interest for electrochemical energy storage because of its high theoretical capacity, natural abundance, and environmental friendliness [12]. However, the electrochemical properties of  $\text{CoMoO}_4$ -based systems remain unsatisfactory because of their intrinsically sluggish reaction kinetics and limited electrochemically active sites, which must be effectively addressed.

In tackling these problems, several approaches have been explored. For instance, surface modification of transition metal oxides has been considered an effective strategy to accelerate and intensify reaction kinetics, realizing high electrochemical performance. A representative example is the recently reported phosphate ion-functionalized  $\text{Co}_3\text{O}_4$  nanosheets [13], whose electrochemically active reaction sites and surface reactivity were efficiently increased, resulting in an improved charge storage capacity. Alternatively, defect engineering by introducing oxygen vacancies or heteroatoms is a promising approach to increase the electrochemically active sites and to improve the reaction kinetics of materials, resulting in enhanced electrochemical performances [14, 15]. For instance, Lu et al. reported that the incorporation of O vacancies into  $\text{Fe}_2\text{O}_3$  exhibited higher electrochemical performance than pure  $\text{Fe}_2\text{O}_3$  [16], which is attributed to the O vacancies serving as shallow donors and

electrochemically active sites, ultimately leading to the accelerated reaction kinetics at the surface. Wang et al. reported that the inclusion of P atoms in  $\text{Co}_3\text{O}_4$  improved the electrocatalytic properties due to the reduced reaction free-energy and the tuned electronic structure after the introduction of the P dopant [17]. As a consequence, simultaneous introduction of P and O vacancies into a lattice structure would be expected to improve energy-storage performance of  $\text{CoMoO}_4$ , but such phenomenon in supercapacitors has been scarcely reported.

Here, we propose a promising strategy to boost the electrochemical performance of  $\text{CoMoO}_4$  nanosheets grown on Ni foam through the introduction of O vacancies and P atoms to the parent material. Density functional theory (DFT) calculations provide insight regarding the contribution of O vacancies and P incorporation on the structural and electronic properties of  $\text{P-CoMoO}_{4-x}$ . The novel  $\text{P-CoMoO}_{4-x}$  exhibits greatly improved electrochemical properties compared to the pristine  $\text{CoMoO}_4$ . Moreover, an assembled asymmetric supercapacitor (ASC) consisting of the optimized  $\text{P-CoMoO}_{4-x}$  as positive electrode and activated carbon (AC) as negative electrode shows a high energy density of  $58 \text{ W h kg}^{-1}$  at a power density of  $850 \text{ W kg}^{-1}$ , and excellent cycling performance with 98.7% capacity retention after 10 000 cycles at a high current density of  $10 \text{ A g}^{-1}$ .

## 2. Results and Discussion

A facile and efficient strategy for the fabrication of P-CoMoO<sub>4-x</sub> nanosheets is proposed (Fig. 1). Typically, CoMoO<sub>4</sub> nanosheets are first grown onto Ni substrate through a facile hydrothermal method followed by a post-annealing treatment. Typical scanning electron microscopy (SEM) images show that Co-Mo precursor nanosheets are fully deposited on the surface of the Ni foam. Magnified SEM images (Fig. S1a and S1b) show that the precursor nanosheets are interconnected with one another and perpendicularly anchored on the Ni substrate, forming hierarchical nanosheet arrays. The magnified view in Fig. S1c shows that the nanosheets have a lateral size of ~600 nm and a thickness of ~20 nm. The interconnectedness and being ultrathin of these nanosheets not only facilitate the ion diffusion but also produce highly exposed electrochemically active sites, which are possibly responsible for high charge storage capacity. After a post-annealing treatment, the Co-Mo precursor is converted into crystalline CoMoO<sub>4</sub>, whose overall hierarchical structures are well preserved (Fig. S1d-S1f). Finally, the obtained CoMoO<sub>4</sub> is further thermally transformed into P-CoMoO<sub>4-x</sub> under flowing Ar in the presence of NaH<sub>2</sub>PO<sub>2</sub>·H<sub>2</sub>O through solid/gas-phase phosphorization. To investigate the effect of phosphorization on the morphology, we used different P source dosages (0.2, 0.4, 0.8, and 1.2 g NaH<sub>2</sub>PO<sub>2</sub>·H<sub>2</sub>O) to synthesize samples denoted as P-CoMoO<sub>4-x-n</sub> ( $n = 1, 2, 3, \text{ and } 4$ ). The corresponding morphological evolution was investigated using SEM (Fig. S2). The P-CoMoO<sub>4-x-1</sub> sample prepared from a low dosage (0.2 g) of P source displays a well-retained overall 3D interconnected network structure (Fig. S2a and S2b), but the

surfaces of the nanosheets have become rough with a small amount of disconnected particles decorated on them. When the P source dosage was increased to 0.4 g, more nanoparticles are deposited on the nanosheets (Fig. S2c and S2d). These nanoparticles become even more obvious when 0.8 g P source was used (Fig. 2a, 2b, S2e, and S2f), producing abundant edge sites derived from small-size effects on the surfaces of the nanosheets [18]. EDS elemental mapping images confirm the existence of Co, Mo, O, and P elements in P-CoMoO<sub>4-x</sub>-3 sample (Fig. S3). With the increase of P source dosage (1.2 g), the interconnected nanosheets become locally jammed (Fig. S2g and S2h), which possibly has reduces the ion-accessible area and impedes electrolyte accessibility, thus limiting the utilization efficiency of the electroactive material. Considering that P-CoMoO<sub>4-x</sub>-3 shows the best electrochemical performance among the studied samples, as discussed below, we characterize this sample in detail.

Structural features of the prepared materials before and after the phosphorization process were further investigated using transmission electron microscopy (TEM). A low-magnification TEM image (Fig. S4a) of CoMoO<sub>4</sub> nanosheet presents a smooth surface, consistent with the SEM results. A high-resolution TEM (HRTEM) image of CoMoO<sub>4</sub> (Fig. S4b) shows that the lattice fringes have a spacing of 0.232 nm, corresponding to the (040) plane of the monoclinic CoMoO<sub>4</sub> phase. A scanning TEM (STEM) image and the corresponding element mapping (Fig. S4c–S4f) reveal homogeneous elemental distribution throughout the nanosheet. For the P-CoMoO<sub>4-x</sub>-3 sample, an individual sheet consists of numerous interconnected nanoparticles (Fig.

2c and 2d). As determined by N<sub>2</sub> adsorption–desorption isotherm (Fig. S5), the P-CoMoO<sub>4-x</sub>-3 shows an increased specific surface area of 113.1 m<sup>2</sup> g<sup>-1</sup> compared to pure CoMoO<sub>4</sub> (49.7 m<sup>2</sup> g<sup>-1</sup>). The P-CoMoO<sub>4-x</sub>-3 and CoMoO<sub>4</sub> show a type-IV isotherm with H3-type hysteresis loops at relative pressure ( $P/P_0$ ) of 0.6–1.0, corresponding to the characteristic of meso-macroporous materials [19], which thus facilitates transport and migration of electrolyte ions within electrode materials [20]. The 2D nanosheet morphology of the P-CoMoO<sub>4-x</sub>-3 offers sufficient electrochemically active sites to facilitate affluent electrochemical reactions [21], which are expected to enhance electrochemical performance. The HRTEM image in Fig. 2e shows two sets of lattice fringes with interplanar distances of 0.223 and 0.309 nm, corresponding to the spacing of the (003) and (310) planes of the CoMoO<sub>4</sub> phase. A magnified view (Fig. 2f) shows a disordered lattice, which is possibly caused by the existence of O vacancies. To examine the presence of oxygen defects in the P-CoMoO<sub>4-x</sub>-3, EPR spectroscopy was carried out. Compared to CoMoO<sub>4</sub>, the P-CoMoO<sub>4-x</sub>-3 exhibits a much higher EPR signal at  $g = 2.005$  (Fig. 2g), corresponding to the unpaired electrons trapped at the site of oxygen vacancies, which is consistent with previous report [22]. The selected area electron diffraction (SAED) pattern of the P-CoMoO<sub>4-x</sub>-3 nanosheet reveals a polycrystalline feature and diffraction rings that correspond to the (400), (310), and (002) planes (Fig. S6). The homogeneous elemental distribution of Co, Mo, O, and P across the P-CoMoO<sub>4-x</sub>-3 structure is confirmed by STEM-EDS mapping images (Fig. 2h).

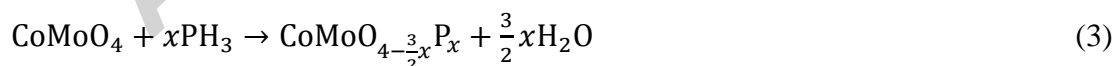
X-ray diffraction (XRD) patterns (Fig. 3a) of both  $\text{CoMoO}_4$  and  $\text{P-CoMoO}_{4-x}$  scraped from the substrate are well indexed to monoclinic  $\text{CoMoO}_4$  (JCPDS: 21-0868) in the  $C2/m$  (No. 12) space group [23], indicating that incorporation of P into  $\text{CoMoO}_4$  lattice does not significantly alter the crystal structure. The peaks of  $\text{P-CoMoO}_{4-x}$  gradually shift to lower diffraction angle compared with those of  $\text{CoMoO}_4$  (Fig. S7a), which is caused by the expansion of the unit cell as a result of the larger atomic radius of P than that of O [24]. The Raman spectra of the as-prepared samples are shown in Fig. 3b. For  $\text{CoMoO}_4$ , the peaks located at  $200\text{--}1200\text{ cm}^{-1}$  can be indexed to characteristic bending and stretching vibrations of  $\alpha\text{-CoMoO}_4$  [23]. Notably, the Raman spectrum of  $\text{P-CoMoO}_{4-x}$  sample matches that of  $\text{CoMoO}_4$ , confirming the successful incorporation of P into the  $\text{CoMoO}_4$  lattice without altering the crystal structure. The Raman peaks gradually become broader, and the peak intensity decreases as P content increases; this phenomenon implies crystallinity degradation, which possibly arises from the formation of defects, such as O vacancies and heteroatom impurities [25]. With increased P content, the peaks of  $\text{P-CoMoO}_{4-x}$  slightly shift to higher wavenumbers compared with those of  $\text{CoMoO}_4$  upon partial P incorporation (Fig. S7b), which is due to a shortening of metal-P distance [26].

X-ray photoelectron spectroscopy (XPS) measurements were conducted to explore the compositional evolution and surface electronic states of  $\text{CoMoO}_4$  nanosheets upon P incorporation. The surface atomic ratios of Co, Mo, O, and P in  $\text{CoMoO}_4$  and  $\text{P-CoMoO}_{4-x}$  samples are listed in Table S1. The O/P atomic ratio gradually decreases

with increased amount of P source during phosphorization. Co/Mo atomic ratios in these samples are approximately 1.0, approaching the stoichiometric ratio for  $\text{CoMoO}_4$ . The binding energies of Co 2p peaks for  $\text{CoMoO}_4$  located at 780.6 and 797.0 eV correspond to Co  $2p_{3/2}$  and Co  $2p_{1/2}$  peaks, indicating the existence of  $\text{Co}^{2+}$  [27]. The observed binding energies for Co  $2p_{3/2}$  and Co  $2p_{1/2}$  levels in the P- $\text{CoMoO}_{4-x}$  samples shift to a higher binding energy compared with those for  $\text{CoMoO}_4$ , and this result is attributed to the high electronegativity P, which reduces the electron density of Co species (Fig. 3c and S8a) [17]. The slight change in the Co 2p spectra suggests that the oxidation state of Co is not affected by P incorporation, consistent with previous results [24, 28]. Besides, two weak peaks in the Co 2p region of all P- $\text{CoMoO}_{4-x}$  samples are observed at 778.5 and 793.5 eV (Fig. 3c), which are ascribed to the local structural distortion induced by P incorporation. The main peak of the Mo 3d binding energy (Fig. 3d) slightly up-shifts from 232.2 eV of  $\text{CoMoO}_4$  to 232.4 eV of P- $\text{CoMoO}_{4-x}$ , along with a shift in the Mo  $2p_{3/2}$  position from 235.4 eV to 235.6 eV, and the splitting width of 3.2 eV in  $\text{CoMoO}_4$  and P- $\text{CoMoO}_{4-x}$  corresponds to  $\text{Mo}^{6+}$  [29]. The broad Mo 3d signal for the P- $\text{CoMoO}_{4-x}$  samples can be deconvoluted into two typical components at 229.6 and 230.4 eV, corresponding to  $\text{Mo}^{4+}$  and  $\text{Mo}^{5+}$  [30, 31]. Notably, a comparison of the integrated area under the fitted curve shows that the atomic ratio for  $\text{Mo}^{6+}/(\text{Mo}^{4+}+\text{Mo}^{5+})$  decreases with increased P-incorporation, indicating the greater formation of low-oxidation-state Mo species (Fig. S8b). Similar studies have shown that redox reactions attributed from

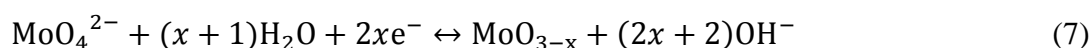
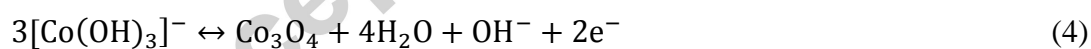
low-oxidation-state Mo species contribute to enhanced electrochemical performance [32-35]. The P 2p core level spectra of the P-CoMoO<sub>4-x</sub> samples present two peak regions (Fig. 3e and S8c), with the regions located around 129.3 and 130.1 eV (P 2p<sub>3/2</sub> and 2p<sub>1/2</sub>, respectively) corresponding to P anions, whereas the other region centered at 134.4 eV is a characteristic of P-O species [36, 37]. The O 1s core-level spectrum (Fig. 3f) of the CoMoO<sub>4</sub> displays four characteristic peaks centered at 530.4, 531.3, 531.9, and 533.0 eV, which can be assigned to the lattice O, hydroxyl group, O defects (O<sub>v</sub>), and physically adsorbed molecular water, respectively [38-40]. In the O 1s spectrum of P-CoMoO<sub>4-x</sub>, two peaks are identified at 531.6 and 532.6 eV, corresponding to the O species of H<sub>2</sub>PO<sub>4</sub><sup>-</sup> and PO<sub>3</sub><sup>-</sup>, which are attributed to the replacement of the hydroxyl group species by the phosphate ion species during phosphorization [13]. It can be observed that the peak density of O<sub>v</sub> component in P-CoMoO<sub>4-x</sub> gradually increases with increased P source (Fig. S8d), indicating the formation of more O vacancies. This finding reveals that metal oxide tends to produce O vacancies in the crystal lattice under a reducing atmosphere, consistent with previous findings [41, 42]. The quantitative atomic contents of the as-synthesized P-CoMoO<sub>4-x</sub> samples were measured using an inductively coupled plasma mass spectrometer (ICP-MS). Table S2 shows that more O vacancies are generated with increased P incorporation into P-CoMoO<sub>4-x</sub>, whereas the atomic ratio of Co/Mo remains constant, which are in good agreement with the XPS results.

On the basis of the above structural analysis of P-CoMoO<sub>4-x</sub>, a possible formation mechanism was proposed. First, NaH<sub>2</sub>PO<sub>2</sub>·H<sub>2</sub>O was decomposed to generate PH<sub>3</sub> vapor by using a thermal annealing process under Ar flow (Equation 1). Given the low hopping barriers and weak metal–O bonds, O vacancies can be induced via reduction of CoMoO<sub>4</sub> [43, 44]. The generated PH<sub>3</sub> acts as a highly active reducing agent that reacts with CoMoO<sub>4</sub> to produce intrinsic O defects in the lattice structure [45, 46]. Hydrolysis of HPO<sub>4</sub><sup>2-</sup> promotes generation of H<sub>2</sub>PO<sub>4</sub><sup>-</sup> at the surface of materials (Equation 2) [47]. The nonequilibrium diffusion process between the outward OH<sup>-</sup> and the inward H<sub>2</sub>PO<sub>4</sub><sup>-</sup> species results in the formation of nanoparticles on the surface of nanosheets, consistent with the nanoscale Kirkendall effect reported in other nanostructures [13, 48]. The formed PH<sub>3</sub> then reacts with CoMoO<sub>4</sub>, forming P-CoMoO<sub>4-x</sub> (Equation 3). From a thermodynamic point of view, dissociation and incorporation of PH<sub>3</sub> as a P-containing species are more favorable in O-deficient CoMoO<sub>4</sub> surface than in pristine CoMoO<sub>4</sub> surface, as revealed by DFT calculations in below (Table S3).



The electrochemical properties of the as-fabricated samples on Ni foam as binder-free electrodes for supercapacitors were investigated in a three-electrode cell configuration, with 1 M KOH as aqueous electrolyte. Fig. 4a compares the cyclic voltammetry (CV)

curves of the  $\text{CoMoO}_4$  and  $\text{P-CoMoO}_{4-x}$  electrodes recorded at a scan rate of  $15 \text{ mV s}^{-1}$  within the potential range of  $0-0.7 \text{ V}$  (vs. saturated calomel electrode (SCE)). It is worth pointing out that the areal capacity contribution from bare Ni foam to  $\text{P-CoMoO}_{4-x}$ -3 electrode is about 3.49%, which is negligible (Fig. S9). A pair of redox peaks with an anodic peak at  $\sim 0.57 \text{ V}$  (vs. SCE) and a cathodic peak at  $\sim 0.30 \text{ V}$  (vs. SCE) is observed in the CV curve of  $\text{CoMoO}_4$ , which is ascribed to the Faradaic redox reactions of  $\text{Co}^{2+}/\text{Co}^{3+}/\text{Co}^{4+}$  associated with  $\text{OH}^-$  [49, 50]. Obviously, the  $\text{P-CoMoO}_{4-x}$  samples show a larger CV integration area than pristine  $\text{CoMoO}_4$  at the same scan rate, and  $\text{P-CoMoO}_{4-x}$ -3 exhibits the largest enclosed CV area. The pronounced enhancement of energy-storage capacity for  $\text{P-CoMoO}_{4-x}$  can be attributed to available redox couples of  $\text{Mo}^{4+}/\text{Mo}^{5+}/\text{Mo}^{6+}$  with an anodic peak at  $\sim 0.29 \text{ V}$  (vs. SCE) and a cathodic peak at  $\sim 0.17 \text{ V}$  (vs. SCE) provided by the reduced Mo species, which are consistent with previous findings [32, 51, 52]. Accordingly, the electrochemical Faradaic reactions of  $\text{P-CoMoO}_{4-x}$  materials can be illustrated by the below equations [32, 49, 50, 52, 53].



The redox reaction reactants of Co and Mo species are based on the Pourbaix diagram, which was reported in literature [23]. The Pourbaix diagram maps out possible stable

equilibrium phases of an aqueous electrochemical system and can be used for dynamic analysis. In our prepared P-CoMoO<sub>4-x</sub>, the pH is 14 and the potential range is 0 to 0.7 V (vs. SCE), the Co element at the interface of electrode and electrolyte will be present in the form of [Co(OH)<sub>3</sub>]<sup>-</sup> and Co<sub>3</sub>O<sub>4</sub>. The Mo element at the interface of electrode and electrolyte will be present in the form of MoO<sub>4</sub><sup>2-</sup>.

The CV curves of CoMoO<sub>4</sub> and various P-CoMoO<sub>4-x</sub> electrodes collected at different scan rates are presented in Fig. 4b and S10. These CV curves are somewhat asymmetric with increased scan rate, and this result is ascribed to the undesired resistance of the electrode materials [54]. To further investigate the charge storage mechanism of as-synthesized samples, we evaluated the relationship between cathodic peak response ( $i_p$ ) and scan rate ( $v$ ) by using the power law ( $i_p = a \cdot v^b$ ) [55].  $b$  can be determined from the slope of  $\log(v)$ – $\log(i_p)$  plot. Typically,  $b = 0.5$  represents a diffusion-controlled current response, whereas  $b = 1.0$  indicates a surface-controlled process. As shown in Fig. 4c, the calculated  $b$ -values for CoMoO<sub>4</sub> and P-CoMoO<sub>4-x-n</sub> ( $n = 1, 2, 3, \text{ and } 4$ ) are in the range of 0.539–0.616, which are close to 0.5, indicating the dominant diffusion-controlled behavior. This is in good agreement with previous reports on the nature of battery-type materials [55]. The largest  $b$ -value of the P-CoMoO<sub>4-x-3</sub> among other samples suggests that P-CoMoO<sub>4-x-3</sub> possesses the fastest reaction kinetics, signifying the prominent electrochemical performance.

Galvanostatic charge–discharge (GCD) tests for  $\text{CoMoO}_4$  and  $\text{P-CoMoO}_{4-x-n}$  ( $n = 1, 2, 3,$  and  $4$ ) electrodes were conducted at different charge–discharge current densities (Fig. 4d and S11). The GCD curves at various current densities are nearly symmetric, indicative of the highly reversible and fast responses of the electrodes. The discharge time of  $\text{P-CoMoO}_{4-x}$  increases with increased P source content (Fig. 4e) until the optimal usage of P source (0.8 g). The discharge time of  $\text{P-CoMoO}_{4-x-4}$  decreases due to surface aggregation caused by excessive phosphorization (Fig. S2g and S2h), which in turn reduces utilization rate of electroactive materials. The calculated specific capacities of the pristine  $\text{CoMoO}_4$  and  $\text{P-CoMoO}_{4-x-n}$  ( $n = 1, 2, 3,$  and  $4$ ) based on GCD curves at a current density of  $2 \text{ A g}^{-1}$  are 651, 884, 985, 1368, and  $1106 \text{ C g}^{-1}$ , respectively (Fig. 4f). Notably, the optimized  $\text{P-CoMoO}_{4-x}$  electrode delivers a maximum specific capacity of  $1368 \text{ C g}^{-1}$  that exceeds the theoretical Faradaic capacity value ( $979.4 \text{ C g}^{-1}$  at a potential window of  $0.6 \text{ vs. SCE/V}$ ; Calculation details in Supporting Information). The ultra-high capacity is attributed to the  $\text{P-CoMoO}_{4-x}$  nanostructure possessing highly exposed active sites and abundant mesoporous (Fig. S5) that enable high contact area between the active materials and the electrolyte and lead to rapid ion/electron transports [56]. As a result, the  $\text{P-CoMoO}_{4-x}$  nanostructure could fully benefit from charge contributions of both Faradaic and non-Faradaic processes. The significant enhancement of specific capacity of  $\text{P-CoMoO}_{4-x}$  indicates that the simultaneous incorporation of O vacancies and P atoms into the lattice of  $\text{CoMoO}_4$  plays a critical role in charge-storage capacity.

When the current density increases from  $2 \text{ A g}^{-1}$  to  $20 \text{ A g}^{-1}$ , the P-CoMoO<sub>4-x-n</sub> ( $n = 1, 2, 3,$  and  $4$ ) electrodes retain high specific capacities of 409, 545, 833, and  $672 \text{ C g}^{-1}$ , respectively. Notably, the superior specific capacity of the optimized P-CoMoO<sub>4-x</sub> is highly competitive with those of the most previously reported CoMoO<sub>4</sub>-based materials (Table S4).

Cycling performance was evaluated by successive GCD tests performed at a high current density of  $10 \text{ A g}^{-1}$  for 5000 cycles (Fig. 4g). The P-CoMoO<sub>4-x-3</sub> exhibits a superior cycling stability, with 95.3% retention of the initial capacity after the cycling test; by contrast, the capacity retention of the pristine CoMoO<sub>4</sub> electrode is 85.9% after the same number of cycles. As shown in Fig. S12, the P-CoMoO<sub>4-x-3</sub> retains a Coulombic efficiency of  $\sim 97.9\%$  during the entire cycling process; this value is higher than that of CoMoO<sub>4</sub> ( $\sim 91.4\%$ ) possibly due to the increased electrical conductivity of P-CoMoO<sub>4-x-3</sub>. The cycling stability is verified from the SEM images of the samples obtained after the cycling measurements (Fig. S13); the images show that the morphology and structural integrity of the P-CoMoO<sub>4-x-3</sub> are well maintained. By contrast, the structure of the pristine CoMoO<sub>4</sub> suffers from obvious pulverization and agglomeration, leading to the loss of electrochemical contact and fast capacity fade. Electrochemical impedance spectroscopy (EIS) was performed to further explore the reaction kinetics of the studied electrodes, and the obtained Nyquist plots are presented in Fig. 4h. The Nyquist plot consists of three main distinguishable regions: high-frequency semicircle, mid-frequency Warburg impedance, and low-frequency

capacitive behaviour (Fig. S14) [57]. The measured impedance data are analyzed by fitting to an equivalent electrical circuit, which is composed of equivalent series resistance ( $R_s$ ), charge-transfer resistance ( $R_{ct}$ ), constant-phase element (CPE), and Warburg impedance (W). The  $R_s$  includes the intrinsic resistance of active materials, ionic resistance of electrolyte, and contact resistance at the active material/current collector interface [58]. The diameter of the semicircle corresponding to  $R_{ct}$  displays the charge-transfer process at the electrode-electrolyte interface [59]. Meanwhile, the W is associated with the electrolyte ion diffusion length and diffusivity within electroactive materials [57]. The fitting parameters for both electrodes are obtained using the equivalent circuit, as summarized in Table S5. The P-CoMoO<sub>4-x</sub>-3 displays smaller  $R_s$  ( $0.85 \Omega \text{ cm}^2$ ) and  $R_{ct}$  ( $0.97 \Omega \text{ cm}^2$ ) than those of the pristine CoMoO<sub>4</sub>, implying higher electrical conductivity and faster charge transfer. The optical band gaps of the CoMoO<sub>4</sub> and P-CoMoO<sub>4-x</sub>-3 are  $\sim 2.01$  and  $1.22$  eV, respectively (Fig. S15), which were measured using UV-VIS-NIR absorption spectra. The reduced band gap value of P-CoMoO<sub>4-x</sub>-3 indicates a high electrical conductivity, which is favorable for the enhancement of electrochemical performance. The EIS results for CoMoO<sub>4</sub> show an obvious increase in  $R_{ct}$  before and after the cycling tests (Fig. S16a), whereas the resistance of P-CoMoO<sub>4-x</sub>-3 has slightly changed after cycling (Fig. S16b). The increased of  $R_{ct}$  of the samples after cycling test is possibly ascribed to the loss of adhesion of electrochemically active materials with the current collector and

agglomeration of electrochemically active materials upon long-term cycling (Fig. S13), resulting in the decreased charge-transfer kinetics.

To better understand the roles of oxygen vacancies and P heteroatoms in the electrochemical performance of P-CoMoO<sub>4-x</sub> structure, we performed DFT calculations to investigate the local atomic environment. Fig. S17 and S18 show the ball-and-stick models of the atomic structure of CoMoO<sub>4</sub> and P-CoMoO<sub>4-x</sub>, respectively. These models show that P atom in P-CoMoO<sub>4-x</sub> is surrounded by the four nearest neighboring O atoms and the six next nearest neighboring transition metal atoms (Fig. S18). That is, the P atom in P-CoMoO<sub>4-x</sub> forms a PO<sub>4</sub> cluster and thus possesses a phosphate-like chemical characteristic, although the PO<sub>4</sub> does not form a standard tetrahedral structure. The lower electronegativity of phosphate ion relative to oxygen ion that results in decreasing energy for the electron transport during the redox reaction [13]. Three Co-O bond lengths (2.03, 2.08, and 2.16 Å) are observed in the pristine CoMoO<sub>4</sub> (Fig. S17), and these Co-O bonds become elongated (2.09, 2.16, and 2.19 Å) after P incorporation. The increased bond length in Co-O that leads to the weakening of the attraction for the 3d electrons of Co<sup>2+</sup> or Co<sup>3+</sup> in CoMoO<sub>4</sub>, and thus providing enhanced surface reactivity and electrochemical reaction kinetics.

To gain insight into the influence of the P incorporation on electronic structure of P-CoMoO<sub>4-x</sub>, we analyzed the optimal lattice parameters and the formation energies of CoMoO<sub>4</sub> and P-CoMoO<sub>4-x</sub>, as summarized in Table S3. The structural analysis reveals that two types of O atoms exist in the lattice of CoMoO<sub>4</sub> (Fig. S17), namely, 2-

and 4-coordinated O atoms. The formation of O vacancies at 2-coordinated O sites is energetically more favorable than that at 4-coordinated O sites. Furthermore, the O vacancy-formation energy of P-CoMoO<sub>4-x</sub> is 2.76 eV, which is lower than that of CoMoO<sub>4-x</sub> (3.23 eV), suggesting that formation of O vacancies is more energetically favored in P-incorporated CoMoO<sub>4</sub> than in CoMoO<sub>4</sub> (Fig. S19 and Table S3). Moreover, the *a*-axis constant increases substantially from 9.87 Å to 10.62 Å upon P incorporation, whereas the *c*-axis constant decreases from 7.83 Å to 7.43 Å. Consequently, the unit cell volume increases from 628.24 Å<sup>3</sup> to 659.74 Å<sup>3</sup> upon P incorporation, and this phenomenon is expected to increase the diffusion kinetics of electrolyte ions within the electrode materials, and thus boost the electrochemical performance of the electrode material. The results are supported by the previous studies. For example, Lee et al. reported that TiNb<sub>6</sub>O<sub>17</sub> exhibited a larger unit cell, which enabled more open lithium insertion/insertion sites and better lithium diffusion coefficients than TiNb<sub>2</sub>O<sub>7</sub> [60]. Similarly, Lou et al. reported that FeNb<sub>11</sub>O<sub>27.9</sub> resulted in a larger unit-cell volume than FeNb<sub>11</sub>O<sub>29</sub>, which facilitated numerous and larger Li<sup>+</sup> ion transport paths in FeNb<sub>11</sub>O<sub>27.9</sub>, thus leading to a higher Li<sup>+</sup> ion diffusion coefficient [61].

To analyze the effect of P incorporation on the oxidation states of Co and Mo, we further studied the projected density of states (DOS) of the Co-3d and Mo-4d states. We found that the electronic configuration of the Co-3d state is  $t_{2g}^3(\uparrow)e_g^2(\uparrow)t_{2g}^2(\downarrow)$  for both P-containing and P-free cases (Fig. 5a and 5b), illustrating that Co atoms

always possess a magnetic moment of  $3 \mu_B$  and an oxidation state of +2. Moreover, the electronic structure of Co atoms is not changed either by O vacancy introduction or P incorporation into  $\text{CoMoO}_4$  (Fig. S19). P incorporation into  $\text{CoMoO}_4$  elongates the Co-O bonds (Fig. S17 and S18) and lowers the Co-O bond energy, resulting in improved surface redox chemistry [62], which imparts favorable electrochemical properties to  $\text{P-CoMoO}_{4-x}$ . However, substantial changes in PDOS are observed in the 4d states (Fig. 5c and 5d) of the Mo atoms close to the P atoms. In  $\text{CoMoO}_4$ , Mo atoms are present as  $\text{Mo}^{6+}$  with all 4d states empty in both spin channels, and all magnetic moments for Mo atoms are zero. In  $\text{P-CoMoO}_{4-x}$ , the oxidation state of the Mo atoms neighboring the P atoms is reduced because some filled Mo-4d orbitals are located below the Fermi level. The magnetic moments of Mo atoms neighboring the P atoms are changed to 1 or  $2 \mu_B$ , corresponding to  $\text{Mo}^{5+}$  or  $\text{Mo}^{4+}$ . These findings are consistent with the XPS results. The filled Mo-4d states appear as impurity states with their energy levels located within the band gap of  $\text{CoMoO}_4$ . As a result, P incorporation substantially decreases the band gap via these impurity states; thus, electronic conductivity can be improved through P incorporation. The calculated total DOS (Fig. 5e) shows that the pristine  $\text{CoMoO}_4$  is a semiconductor with an energy gap of 2.18 eV. After O vacancies are created, the energy gap decreases to 1.29 eV (Fig. S20), and the impurity states remain below the Fermi level. Upon P incorporation, the band gap is further reduced to 1.09 eV because more impurity states appear in the band gap (Fig. 5f). We further examined the electrical properties of as-synthesized

samples using four-probe techniques. The P-CoMoO<sub>4-x</sub>-3 shows higher electrical conductivity ( $3.9 \times 10^{-2} \text{ S m}^{-1}$ ) than pure CoMoO<sub>4</sub> ( $5.7 \times 10^{-3} \text{ S m}^{-1}$ ), which facilitates electron transport, thus enabling fast reaction kinetics. These results further explain why P-CoMoO<sub>4-x</sub> performs enhanced electrochemical performances.

To evaluate the electrochemical properties of the P-CoMoO<sub>4-x</sub> for real applications, we assembled a two-electrode configuration by using P-CoMoO<sub>4-x</sub>-3 as the positive electrode material and AC as the negative electrode material (Fig. S21) in 1 M KOH aqueous electrolyte with cellulosic paper as separator (Fig. 6a). To achieve the maximum voltage window and the best electrochemical performance of the ASC device, we adjusted the mass ratio of P-CoMoO<sub>4-x</sub>-3 to AC to ~0.23 according to the CV curves obtained at a scan rate of  $10 \text{ mV s}^{-1}$  (Fig. S22). The CV curves (Fig. 6b) of the P-CoMoO<sub>4-x</sub>-3//AC device at different voltage windows at a scan rate of  $30 \text{ mV s}^{-1}$  show a quasi-rectangular behavior even at the voltage window of up to 1.7 V, indicating the feasibility of employing P-CoMoO<sub>4-x</sub>-3 and AC as negative and positive electrode materials, respectively [63]. Various GCD curves (Fig. 6c) of the device collected at different voltage windows at  $1 \text{ A g}^{-1}$  display a quasi-triangular shape, signifying the good electrochemical reversibility. However, when the voltage window is wider than 1.7 V, the GCD curve becomes less symmetrical, indicating a reduction in the reversibility of the ASC device. Therefore, the stable operating voltage can be extended up to 1.7 V. The CV curves of the device were obtained at various scan rates (Fig. 6d). The shapes of the CV curves remain undistorted with increased scan rate,

suggesting a superior rate performance that can be attributed to the fast ionic and electronic transport dynamics of the electrode materials [54]. For comparison, a reference ASC device was assembled using  $\text{CoMoO}_4$  and AC as the positive and negative electrode materials, respectively. The mass ratio of  $\text{CoMoO}_4$  to AC was  $\sim 0.43$  according to their individual electrochemical behaviors (Fig. S23a). The GCD curves obtained using the P- $\text{CoMoO}_{4-x-3}$ //AC display a more symmetrical shape compared with that obtained using the  $\text{CoMoO}_4$ //AC at different current densities (Fig. 6e and S23b); this result demonstrates the enhanced electrochemical reversibility of the P- $\text{CoMoO}_{4-x-3}$ //AC.

The specific capacities calculated from GCD curves are presented in Fig. 6f. The specific capacity of the P- $\text{CoMoO}_{4-x-3}$ //AC is  $220 \text{ C g}^{-1}$  at a current density of  $1 \text{ A g}^{-1}$ , which is higher than that of the  $\text{CoMoO}_4$ //AC ( $156 \text{ C g}^{-1}$ ) at the same current density (Fig. S23c). Notably, the P- $\text{CoMoO}_{4-x-3}$ //AC retains a specific capacity of  $71 \text{ C g}^{-1}$  even at a high current density of  $15 \text{ A g}^{-1}$ . Energy and power densities are two important indicators used to evaluate the electrochemical performance of supercapacitor technologies. According to the Ragone plot derived from the GCD curves of the P- $\text{CoMoO}_{4-x-3}$ //AC (Fig. 6g), the device delivers a favorable energy density of  $58 \text{ W h kg}^{-1}$  at a power density of  $850 \text{ W kg}^{-1}$ , and it maintains an energy density of  $18.8 \text{ W h kg}^{-1}$  even at a high power density of  $12\,750 \text{ W kg}^{-1}$ . By contrast, the energy density of the  $\text{CoMoO}_4$ //AC decreases from  $40.8 \text{ W h kg}^{-1}$  to  $10.2 \text{ W h kg}^{-1}$  as the power density increases from  $850 \text{ W h kg}^{-1}$  to  $12\,750 \text{ W kg}^{-1}$  (Fig. S23d).

Furthermore, the high energy and power densities achieved for the P-CoMoO<sub>4-x</sub>-3//AC considerably exceed those of the reported CoMoO<sub>4</sub>-based ASC devices, such as  $\alpha$ -CoMoO<sub>4</sub>//AC [64], Co<sub>3</sub>O<sub>4</sub>@CoMoO<sub>4</sub>//AC [65], CoMoO<sub>4</sub>@Co<sub>3</sub>O<sub>4</sub>//AC [53], CoMoO<sub>4</sub>-3D graphene foam//AC [49], CoMoO<sub>4</sub>-NiMoO<sub>4</sub>·xH<sub>2</sub>O//AC [66], and CoMoO<sub>4</sub>-NiMoO<sub>4</sub>//AC [67]. The cycling stability of the P-CoMoO<sub>4-x</sub>-3//AC was measured at a high current density of 10 A g<sup>-1</sup> for 10 000 continuous charge–discharge cycles (Fig. 6h). Remarkably, 98.7% of the initial capacity is retained after cycling test, illustrating the excellent cycling stability of the constructed device. The obtained value for the cycling performance is worth emphasizing and is way higher than that of the reported ASC devices with CoMoO<sub>4</sub>-based composites [49, 65, 68]. Moreover, Coulombic efficiency gradually increases over the first 1200 cycles and is maintained above 91.6% during the cycling test (Fig. S24). The EIS plots of the P-CoMoO<sub>4-x</sub>-3//AC show a slight change before and after cycling tests (Fig. S25), confirming the high cycling stability of our assembled device. Moreover, a good cycling performance is further demonstrated with the ~95.8% capacity retention after the same number of cycles at a high current density of 15 A g<sup>-1</sup>, with high Coulombic efficiency of ~98.9% during cycles (Fig. S26).

### 3. Conclusions

We have demonstrated a facile strategy for creating O vacancies and incorporating P atoms in P-CoMoO<sub>4-x</sub> nanosheets on conductive Ni foam. Experimental and

theoretical studies provide insight into the effect of the introduction of P and of O vacancies on structural and electrical properties of P-CoMoO<sub>4-x</sub>. Moreover, P incorporation into the P-CoMoO<sub>4-x</sub> lattice induces reduction in bond energy of Co-O and the formation of Mo species with a lower oxidation state, resulting in substantially enhanced redox reaction kinetics and electrochemical performance. Additionally, the resulting 2D nanosheets decorated by the abundant nanoparticles are chemically self-assembled on the conductive substrate, which not only provide reduced path lengths for ion diffusion but also avoid “dead volume” caused by the addition of conductive agents and polymer binders. Owing to its superior features, the optimized P-CoMoO<sub>4-x</sub> achieves a high specific capacity of 1368 C g<sup>-1</sup> at a current density of 2 A g<sup>-1</sup>, as well as excellent rate capability and electrochemical stability. The asymmetric supercapacitor P-CoMoO<sub>4-x</sub>//AC delivers superior energy densities of 58 and 18.8 W h kg<sup>-1</sup> at power densities of 850 and 12 750 W kg<sup>-1</sup>, respectively, while maintaining an ultra-long cycle life (98.7% retention after 10 000 cycles at 10 A g<sup>-1</sup>). The proposed strategy may serve as guide in tuning intrinsic electrical properties and in designing structural configuration of other electrode materials for electrochemical storage applications.

## Notes

The authors declare no competing financial interest.

## 4. Experimental Section

### 4.1. Material Synthesis

All reagents were of analytical grade and used as received without further purification. Prior to the preparation of  $\text{CoMoO}_4$ , two pieces of Ni foam ( $2\text{ cm} \times 3\text{ cm}$ ) were cleaned ultrasonically for 10 min with 3 M HCl solution, ethanol, and deionized water in sequence to remove the surface oxide layer and oil contamination. In a typical synthesis, 2 mmol each of  $\text{Co}(\text{NO}_3)_2 \cdot 6\text{H}_2\text{O}$  and  $\text{Na}_2\text{MoO}_4 \cdot 7\text{H}_2\text{O}$  were dissolved in 80 mL of deionized water under magnetic stirring to form a homogeneous pink solution. The pretreated Ni foam and reaction solution were subsequently transferred into a 100 mL Teflon-lined stainless-steel autoclave. The autoclave was sealed and maintained at  $160\text{ }^\circ\text{C}$  for 10 h and then allowed to cool to room temperature. The Ni foam with attached products was rinsed with distilled water and ethanol for several times and subsequently dried under vacuum at  $80\text{ }^\circ\text{C}$  for 12 h. The dried products were finally calcined at  $350\text{ }^\circ\text{C}$  for 2 h at a ramp rate of  $5\text{ }^\circ\text{C min}^{-1}$  under Ar atmosphere. To prepare P- $\text{CoMoO}_{4-x}$ , a porcelain boat filled with  $\text{NaH}_2\text{PO}_2 \cdot \text{H}_2\text{O}$  was placed at the upstream side of a tube furnace. The other porcelain boat loaded with Ni foam supporting the obtained products was placed at the downstream side.  $\text{NaH}_2\text{PO}_2 \cdot \text{H}_2\text{O}$  was used as a precursor to generate  $\text{PH}_3$  via thermal decomposition. A series of P- $\text{CoMoO}_{4-x-n}$  ( $n = 1, 2, 3, \text{ and } 4$ ) samples were obtained using different amounts of  $\text{NaH}_2\text{PO}_2 \cdot \text{H}_2\text{O}$ , that is,  $n = 0.2, 0.4, 0.8, \text{ and } 1.2\text{ g}$  through a solid/gas-phase reaction involving  $\text{CoMoO}_4$  and  $\text{PH}_3$  reactants; the reaction was

conducted at 400 °C for 2 h at a ramp rate of 5 °C min<sup>-1</sup> under the flow of Ar gas. For comparison, CoMoO<sub>4</sub> was prepared under the same condition without P source.

#### 4.2. Material Characterization

The crystalline structure of the materials was characterized using a Rigaku Ultima X-ray diffractometer with Cu K $\alpha$  radiation (XRD; SmartLab;  $\lambda=1.5418$  Å). Morphological and structural characterizations were performed using FESEM (JEOL-7800F; JEOL) and TEM (JEM-2010; JEOL) equipped with an energy-dispersive X-ray spectrometer operated at 200 kV. Raman spectroscopy was conducted on a micro-Raman spectrometer LabRAM HR with a laser excitation wavelength of 514.5 nm. XPS (Thermo Scientific ESCALAB 250; Thermo UK) measurements were performed with monochromatic Al K $\alpha$  radiation as radiation source to investigate the surface states. The elemental composition of the samples was determined by an inductively coupled plasma mass spectroscope (ICP-MS Agilent 7900, Tokyo, Japan). The optical band gaps of the samples were measured from UV–Vis–NIR absorption spectra (Agilent Cary 5000). Electron paramagnetic resonance (EPR) analysis was carried out using a Bruker EMX/Plus spectrometer equipped with a dual-mode cavity (ER 4116DM). The electrical conductivities of the sample pellets compressed from prepared powder were analyzed by a four-probe method using an electrometer (Keithley Model 2612). The specific surface area and pore size distribution were measured by an Autosorb-iQ 2ST/MP physisorption analyzer with nitrogen as an adsorptive agent at 77 K.

### 4.3. Electrochemical Measurements

The electrochemical behavior of the samples was investigated using an Ivium-n-Stat electrochemical workstation (Ivium, Netherlands) in three-electrode mode in 1 M KOH electrolyte. The as-prepared samples ( $1 \times 1 \text{ cm}^2$ ) were used directly as the working electrodes. The masses of the pristine  $\text{CoMoO}_4$  and P- $\text{CoMoO}_{4-x-n}$  ( $n = 1, 2, 3$ , and 4) weighted before and after the loading on Ni foam were approximately  $3.2$  and  $3.4 \text{ mg cm}^{-2}$ , respectively. Platinum sheet and SCE were used as counter and reference electrodes, respectively. EIS measurements were recorded at the frequency range of  $100 \text{ kHz}$  to  $0.01 \text{ Hz}$  with an alternating current amplitude of  $5 \text{ mV}$  at the open circuit potential. Specific capacity ( $Q_s, \text{ C g}^{-1}$ ) was calculated from the charge-discharge profiles using the following equation [69].

$$Q_s = \frac{I \int_0^{\Delta t} V dt}{m \times \Delta V_{mean}} = \frac{I \int_0^{\Delta t} V dt}{m \times \frac{\Delta V}{2}} = 2 \frac{I \int_0^{\Delta t} V dt}{m \Delta V}, \quad (8)$$

where  $I$ ,  $\Delta t$ ,  $V$ ,  $\Delta V_{mean}$ ,  $m$ , and  $\Delta V$  are the discharge current (A), discharge time (s), operating potential (V), mean value of operating potential (V), mass (g), and potential window (V) of electroactive materials, respectively.

The negative electrode was prepared through slurry-coating onto Ni foam. The slurry comprised activated carbon (AC), acetylene black, and polyvinylidene fluoride at a weight ratio of 85:10:5 and dissolved in *N*-methyl pyrrolidone. Prior to the assembly of the device, the masses of the positive ( $m_+$ ) and negative electrode materials ( $m_-$ ) were balanced according to charge balance theory (Equation 9).

$$\frac{m_+}{m_-} = \frac{C_- \times \Delta V_-}{Q_+} \quad (9)$$

where  $Q_+$ ,  $C_-$ , and  $\Delta V_-$  are the specific capacity of the positive electrode, the specific capacitance and potential window of AC electrode, respectively.

For the fabrication of ASC device, the optimized P-CoMoO<sub>4-x</sub>-3 (3.4 mg in 1×1 cm<sup>2</sup>) and AC (18.2 mg in 1×1 cm<sup>2</sup>) were used as the positive and negative electrode materials, respectively; a piece of cellulose paper was used as separator to assemble a coin cell. Specific capacity ( $Q_d$ , C g<sup>-1</sup>), energy density ( $E$ , W h kg<sup>-1</sup>) and power density ( $P$ , W kg<sup>-1</sup>) of device were calculated from current charging/discharging curves using the following equations, respectively [69, 70].

$$Q_d = 2 \frac{I \int_0^{\Delta t_s} V_s dt}{M \Delta V_s} \quad (10)$$

$$E = \frac{I \int_0^{\Delta t_s} V_s dt}{3.6 \cdot M} \quad (11)$$

$$P = \frac{3600 \cdot E}{\Delta t_s} \quad (12)$$

where  $I$ ,  $M$ ,  $\Delta t_s$ ,  $V_s$  and  $\Delta V_s$  are the discharge current (A), the total mass of the positive and negative electrode materials (g), discharge time (s), operating voltage (V), and voltage window (V) of the discharge process, respectively.

#### 4.4. Density Functional Theory Calculations

DFT calculations were performed using the Vienna *ab initio* simulation package [71]. Core-ion and valence-electron interactions were described using the projector augmented wave method [72], whereas the electron exchange-correlation interactions were described using the spin-polarized generalized gradient approximation Perdew-Burke-Ernzerh function [73]. A Hubbard U-term was used to determine the Co-3d and Mo-4d states, and the selected effective U values were 4.41 and 4.50 eV for Co and Mo, respectively [74]. The lattice parameters and atomic positions were fully

relaxed, and the final force of all relaxed atoms was less than  $0.05 \text{ eV } \text{\AA}^{-1}$ . The Monkhorst–Pack scheme with a  $3 \times 3 \times 3$   $k$ -point mesh was used for the integration in the irreducible Brillouin zone [75]. The selected cut-off energy of the plane waves was 520 eV. DOS smearing was achieved using the Gaussian smearing method with a smearing width of 0.05 eV. Here, we provide a short description of the theoretical calculations. The unit cell of  $\text{CoMoO}_4$  contains 8 Co atoms, 8 Mo atoms, and 32 O atoms. For the model of  $\text{CoMoO}_{4-x}$  with O vacancies, one O atom was removed from the unit cell for band gap calculation. The concentration of the O vacancy is  $1/32$  ( $x$  value in  $\text{CoMoO}_{4-x}$  is  $1/8$ ).

## References

- [1] P. Zhang, B.Y. Guan, L. Yu, X.W.D. Lou, Formation of Double- Shelled Zinc–Cobalt Sulfide Dodecahedral Cages from Bimetallic Zeolitic Imidazolate Frameworks for Hybrid Supercapacitors, *Angew. Chem., Int. Ed.*, 56 (2017) 7141-7145.
- [2] J.A. Syed, J. Ma, B. Zhu, S. Tang, X. Meng, Hierarchical Multicomponent Electrode with Interlaced  $\text{Ni}(\text{OH})_2$  Nanoflakes Wrapped Zinc Cobalt Sulfide Nanotube Arrays for Sustainable High- Performance Supercapacitors, *Adv. Energy Mater.*, 7 (2017) 1701228.
- [3] K.A. Owusu, L. Qu, J. Li, Z. Wang, K. Zhao, C. Yang, K.M. Hercule, C. Lin, C. Shi, Q. Wei, Low-crystalline iron oxide hydroxide nanoparticle anode for high-performance supercapacitors, *Nat. Commun.*, 8 (2017) 14264.
- [4] P. Ratajczak, M.E. Suss, F. Kaasik, F. Béguin, Carbon electrodes for capacitive technologies, *Energy Storage Mater.*, 16 (2018) 126-145.
- [5] M. Li, Y. Wang, H. Yang, P.K. Chu, Hierarchical  $\text{CoMoO}_4@ \text{Co}_3\text{O}_4$  nanocomposites on an ordered macro-porous electrode plate as a multi-dimensional

electrode in high-performance supercapacitors, *J. Mater. Chem. A*, 5 (2017) 17312-17324.

[6] X. Wu, Q. Wang, W. Zhang, Y. Wang, W. Chen, Nanorod structure of Polypyrrole-covered  $\text{MoO}_3$  for supercapacitors with excellent cycling stability, *Mater. Lett.*, 182 (2016) 121-124.

[7] T. Deng, W. Zhang, O. Arcelus, J.-G. Kim, J. Carrasco, S.J. Yoo, W. Zheng, J. Wang, H. Tian, H. Zhang, Atomic-level energy storage mechanism of cobalt hydroxide electrode for pseudocapacitors, *Nat. Commun.*, 8 (2017) 15194.

[8] S. Li, Y. Chang, J. Yang, Z. Changtai, M. Zhang, H. Huang, L. Zhibin, W. Guo, J. Qiu, Superhydrophilic “Nanoglue” Stabilizing the Metal Hydroxides onto Carbon Materials for High-Energy and Ultralong-Life Asymmetric Supercapacitors, *Energy Environ. Sci.*, 10 (2017) 1958-1965.

[9] S. Peng, L. Li, H.B. Wu, S. Madhavi, X.W.D. Lou, Controlled growth of  $\text{NiMoO}_4$  nanosheet and nanorod arrays on various conductive substrates as advanced electrodes for asymmetric supercapacitors, *Adv. Energy Mater.*, 5 (2015) 1-7.

[10] Y. Guo, L. Yu, C.Y. Wang, Z. Lin, X.W.D. Lou, Hierarchical Tubular Structures Composed of Mn- Based Mixed Metal Oxide Nanoflakes with Enhanced Electrochemical Properties, *Adv. Funct. Mater.*, 25 (2015) 5184-5189.

[11] L. Yu, B. Guan, W. Xiao, X.W.D. Lou, Formation of Yolk- Shelled Ni-Co Mixed Oxide Nanoprisms with Enhanced Electrochemical Performance for Hybrid Supercapacitors and Lithium Ion Batteries, *Adv. Energy Mater.*, 5 (2015) 1500981.

[12] Y. Chen, Y. Wang, X. Shen, R. Cai, H. Yang, K. Xu, A. Yuan, Z. Ji, Cyanide-metal framework derived  $\text{CoMoO}_4/\text{Co}_3\text{O}_4$  hollow porous octahedrons as advanced anodes for high performance lithium ion batteries, *J. Mater. Chem. A*, 6 (2018) 1048-1056.

[13] T. Zhai, L. Wan, S. Sun, Q. Chen, J. Sun, Q. Xia, H. Xia, Phosphate ion functionalized  $\text{Co}_3\text{O}_4$  ultrathin nanosheets with greatly improved surface reactivity for high performance pseudocapacitors, *Adv. Mater.*, 29 (2017) 1604167.

- [14] H.-S. Kim, J.B. Cook, H. Lin, J.S. Ko, S.H. Tolbert, V. Ozolins, B. Dunn, Oxygen vacancies enhance pseudocapacitive charge storage properties of  $\text{MoO}_{3-x}$ , *Nat. Mater.*, 16 (2017) 454-460.
- [15] Y. Wang, T. Zhou, K. Jiang, P. Da, Z. Peng, J. Tang, B. Kong, W.B. Cai, Z. Yang, G. Zheng, Reduced mesoporous  $\text{Co}_3\text{O}_4$  nanowires as efficient water oxidation electrocatalysts and supercapacitor electrodes, *Adv. Energy Mater.*, 4 (2014) 1400696.
- [16] X. Lu, Y. Zeng, M. Yu, T. Zhai, C. Liang, S. Xie, M.S. Balogun, Y. Tong, Oxygen-deficient hematite nanorods as high-performance and novel negative electrodes for flexible asymmetric supercapacitors, *Adv. Mater.*, 26 (2014) 3148-3155.
- [17] Z. Wang, H. Liu, R. Ge, X. Ren, J. Ren, D. Yang, L. Zhang, X. Sun, Phosphorus-Doped  $\text{Co}_3\text{O}_4$  Nanowire Array: A Highly Efficient Bifunctional Electrocatalyst for Overall Water Splitting, *ACS Catal.*, 8 (2018) 2236-2241.
- [18] W. He, C. Wang, H. Li, X. Deng, X. Xu, T. Zhai, Ultrathin and Porous  $\text{Ni}_3\text{S}_2/\text{CoNi}_2\text{S}_4$  3D-Network Structure for Superhigh Energy Density Asymmetric Supercapacitors, *Adv. Energy Mater.*, 7 (2017) 1700983.
- [19] Y. Pan, Y. Lin, Y. Chen, Y. Liu, C. Liu, Cobalt phosphide-based electrocatalysts: synthesis and phase catalytic activity comparison for hydrogen evolution, *J. Mater. Chem. A*, 4 (2016) 4745-4754.
- [20] J. Yan, W. Sun, T. Wei, Q. Zhang, Z. Fan, F. Wei, Fabrication and electrochemical performances of hierarchical porous  $\text{Ni}(\text{OH})_2$  nanoflakes anchored on graphene sheets, *J. Mater. Chem.*, 22 (2012) 11494-11502.
- [21] Y. Li, J. Xu, T. Feng, Q. Yao, J. Xie, H. Xia,  $\text{Fe}_2\text{O}_3$  Nanoneedles on Ultrafine Nickel Nanotube Arrays as Efficient Anode for High-Performance Asymmetric Supercapacitors, *Adv. Funct. Mater.*, 27 (2017) 1606728
- [22] R. Yang, X. Lu, X. Huang, Z. Chen, X. Zhang, M. Xu, Q. Song, L. Zhu, Bi-component  $\text{Cu}_2\text{O}-\text{CuCl}$  composites with tunable oxygen vacancies and enhanced photocatalytic properties, *Appl. Catal., B.*, 170 (2015) 225-232.

- [23] L. Mai, F. Yang, Y. Zhao, X. Xu, L. Xu, Y. Luo, Hierarchical MnMoO<sub>4</sub>/CoMoO<sub>4</sub> heterostructured nanowires with enhanced supercapacitor performance, *Nat. Commun.*, 2 (2011) 381.
- [24] Z. Wu, X. Li, W. Liu, Y. Zhong, Q. Gan, X. Li, H. Wang, Materials Chemistry of Iron Phosphosulfide Nanoparticles: Synthesis, Solid State Chemistry, Surface Structure and Electrocatalysis for Hydrogen Evolution Reaction, *ACS Catal.*, 7 (2017) 4026-4032.
- [25] Y. Tang, N. Rong, F. Liu, M. Chu, H. Dong, Y. Zhang, P. Xiao, Enhancement of the photoelectrochemical performance of CuWO<sub>4</sub> films for water splitting by hydrogen treatment, *Appl. Surf. Sci.*, 361 (2016) 133-140.
- [26] S. Wang, Z. Xiao, Y. Wang, Y. Huang, C. Dong, J. Ma, S. Shen, Y. Li, Filling the Oxygen Vacancies in Co<sub>3</sub>O<sub>4</sub> with Phosphorus: an Ultra-efficient Electrocatalyst for the Overall Water Splitting, *Energy Environ. Sci.*, 10 (2017) 2563-2569.
- [27] J. Zhao, H. Li, C. Li, Q. Zhang, J. Sun, X. Wang, J. Guo, L. Xie, J. Xie, B. He, MOF for template-directed growth of well-oriented nanowire hybrid arrays on carbon nanotube fibers for wearable electronics integrated with triboelectric nanogenerators, *Nano Energy*, 45 (2018) 420-431.
- [28] K. Xu, H. Ding, M. Zhang, M. Chen, Z. Hao, L. Zhang, C. Wu, Y. Xie, Regulating Water- Reduction Kinetics in Cobalt Phosphide for Enhancing HER Catalytic Activity in Alkaline Solution , *Adv. Mater.*, 29 (2017) 1606980.
- [29] M.Q. Yu, L.X. Jiang, H.G. Yang, Ultrathin nanosheets constructed CoMoO<sub>4</sub> porous flowers with high activity for electrocatalytic oxygen evolution, *Chem comm* , 51 (2015) 14361-14364.
- [30] Y.Y. Chen, Y. Zhang, X. Zhang, T. Tang, H. Luo, S. Niu, Z.H. Dai, L.J. Wan, J.S. Hu, Self- Templated Fabrication of MoNi<sub>4</sub>/MoO<sub>3-x</sub> Nanorod Arrays with Dual Active Components for Highly Efficient Hydrogen Evolution, *Adv. Mater.*, 29 (2017) 1703311.

- [31] W. Tang, C.X. Peng, C.T. Nai, J. Su, Y.P. Liu, M. Reddy, M. Lin, K.P. Loh, Ultrahigh Capacity Due to Multi- Electron Conversion Reaction in Reduced Graphene Oxide- Wrapped MoO<sub>2</sub> Porous Nanobelts, *Small*, 11 (2015) 2446-2453.
- [32] K.M. Hercule, Q. Wei, A.M. Khan, Y. Zhao, X. Tian, L. Mai, Synergistic effect of hierarchical nanostructured MoO<sub>2</sub>/Co(OH)<sub>2</sub> with largely enhanced pseudocapacitor cyclability, *Nano Lett.*, 13 (2013) 5685-5691.
- [33] F.N.I. Sari, J. Ting, MoS<sub>2</sub>/MoO<sub>x</sub> Nanostructure Decorated Activated Carbon Cloth for Enhanced Supercapacitor Performances, *ChemSusChem*, 11 (2018) 897-906.
- [34] K. Tang, Y. Li, Y. Li, H. Cao, Z. Zhang, Y. Zhang, J. Yang, Self-reduced VO/VO<sub>x</sub>/carbon nanofiber composite as binder-free electrode for supercapacitors, *Electrochim. Acta*, 209 (2016) 709-718.
- [35] T. Zhai, S. Xie, M. Yu, P. Fang, C. Liang, X. Lu, Y. Tong, Oxygen vacancies enhancing capacitive properties of MnO<sub>2</sub> nanorods for wearable asymmetric supercapacitors, *Nano Energy*, 8 (2014) 255-263.
- [36] W. Liu, E. Hu, H. Jiang, Y. Xiang, Z. Weng, M. Li, Q. Fan, X. Yu, E.I. Altman, H. Wang, A highly active and stable hydrogen evolution catalyst based on pyrite-structured cobalt phosphosulfide, *Nat. Commun.*, 7 (2016) 1-9.
- [37] A.M. Elshahawy, C. Guan, X. Li, H. Zhang, Y. Hu, H. Wu, S.J. Pennycook, J. Wang, Sulfur-doped cobalt phosphide nanotube arrays for highly stable hybrid supercapacitor, *Nano Energy*, 39 (2017) 162-171.
- [38] F. Wu, Q. Liao, F. Cao, L. Li, Y. Zhang, Non-noble bimetallic NiMoO<sub>4</sub> nanosheets integrated Si photoanodes for highly efficient and stable solar water splitting, *Nano Energy*, 34 (2017) 8-14.
- [39] L. Zhuang, L. Ge, Y. Yang, M. Li, Y. Jia, X. Yao, Z. Zhu, Ultrathin Iron- Cobalt Oxide Nanosheets with Abundant Oxygen Vacancies for the Oxygen Evolution Reaction, *Adv. Mater.*, 29 (2017) 1606793.

- [40] L. Xu, Q. Jiang, Z. Xiao, X. Li, J. Huo, S. Wang, L. Dai, Plasma- Engraved  $\text{Co}_3\text{O}_4$  Nanosheets with Oxygen Vacancies and High Surface Area for the Oxygen Evolution Reaction, *Angew. Chem., Int. Ed.*, 128 (2016) 5363-5367.
- [41] M. Yu, X. Cheng, Y. Zeng, Z. Wang, Y. Tong, X. Lu, S. Yang, Dual- Doped Molybdenum Trioxide Nanowires: A Bifunctional Anode for Fiber- Shaped Asymmetric Supercapacitors and Microbial Fuel Cells, *Angew. Chem., Int. Ed.*, 55 (2016) 6762-6766.
- [42] K. Xiang, Z. Xu, T. Qu, Z. Tian, Y. Zhang, Y. Wang, M. Xie, X. Guo, W. Ding, X. Guo, Two dimensional oxygen-vacancy-rich  $\text{Co}_3\text{O}_4$  nanosheets with excellent supercapacitor performances, *Chem comm*, 53 (2017) 12410-12413.
- [43] J.O. Shim, D.W. Jeong, W.J. Jang, K.W. Jeon, S.H. Kim, B.H. Jeon, H.S. Roh, J.G. Na, Y.K. Oh, S.S. Han, Optimization of unsupported CoMo catalysts for decarboxylation of oleic acid, *Catal. Commun.*, 67 (2015) 16-20.
- [44] M.T. Greiner, L. Chai, M.G. Helander, W.M. Tang, Z.H. Lu, Transition metal oxide work functions: the influence of cation oxidation state and oxygen vacancies, *Adv. Funct. Mater.*, 22 (2012) 4557-4568.
- [45] S.A. Buckler, L. Doll, F.K. Lind, M. Epstein, Phosphine as a reducing agent, *J. Org. Chem.*, 27 (1962) 794-798.
- [46] M. Sataev, P. Abdurasova, S.T. Koshkarbaeva, A. Bolisbek, N. Saripbekova, G. Kambarova, O. Koblanova, S. Perni, P. Prokopovich, A low-temperature gold coating of the dielectric surfaces employing phosphine gas as a reducing agent, *Colloids Surf. A*, 521 (2017) 86-91.
- [47] A. Chennah, Y. Naciri, H.A. Ahsaine, A. Taoufyq, B. Bakiz, L. Bazzi, F. Guinneton, J.-R. Gavarri, A. Benlhachemi, Electrocatalytic properties of hydroxyapatite thin films electrodeposited on stainless steel substrates, *MedJChem.*, 6 (2017) 255-266.
- [48] B.Y. Guan, L. Yu, X. Wang, S. Song, X.W.D. Lou, Formation of Onion- Like  $\text{NiCo}_2\text{S}_4$  Particles via Sequential Ion- Exchange for Hybrid Supercapacitors, *Adv. Mater.*, 29 (2016) 1605051.

- [49] X. Yu, B. Lu, Z. Xu, Super Long- Life Supercapacitors Based on the Construction of Nanohoneycomb- Like Strongly Coupled  $\text{CoMoO}_4$ -3D Graphene Hybrid Electrodes, *Adv. Mater.*, 26 (2014) 1044-1051.
- [50] Z. Gu, R. Wang, H. Nan, B. Geng, X. Zhang, Construction of unique  $\text{Co}_3\text{O}_4$ @ $\text{CoMoO}_4$  core/shell nanowire arrays on Ni foam by the action exchange method for high-performance supercapacitors, *J. Mater. Chem. A*, 3 (2015) 14578-14584.
- [51] K. Zhou, W. Zhou, X. Liu, Y. Sang, S. Ji, W. Li, J. Lu, L. Li, W. Niu, H. Liu, Ultrathin  $\text{MoO}_3$  nanocrystals self-assembled on graphene nanosheets via oxygen bonding as supercapacitor electrodes of high capacitance and long cycle life, *Nano Energy*, 12 (2015) 510-520.
- [52] H. Xuan, Y. Zhang, Y. Xu, H. Li, P. Han, D. Wang, Y. Du, A facile route to large- scale synthesis  $\text{MoO}_2$  and  $\text{MoO}_3$  as electrode materials for high- performance supercapacitors, *Phys. Status Solidi A*, 213 (2016) 2468-2473.
- [53] M. Zhou, F. Lu, X. Shen, W. Xia, H. He, X. Zeng, One-pot construction of three dimensional  $\text{CoMoO}_4/\text{Co}_3\text{O}_4$  hybrid nanostructures and their application in supercapacitors, *J. Mater. Chem. A*, 3 (2015) 21201-21210.
- [54] J. Zhu, S. Tang, J. Wu, X. Shi, B. Zhu, X. Meng, Wearable High- Performance Supercapacitors Based on Silver- Sputtered Textiles with  $\text{FeCo}_2\text{S}_4$ - $\text{NiCo}_2\text{S}_4$  Composite Nanotube- Built Multitripod Architectures as Advanced Flexible Electrodes, *Adv. Energy Mater.*, 7 (2017) 1601234.
- [55] B.Y. Guan, A. Kushima, L. Yu, S. Li, J. Li, X.W.D. Lou, Coordination Polymers Derived General Synthesis of Multishelled Mixed Metal- Oxide Particles for Hybrid Supercapacitors, *Adv. Mater.*, 29 (2017) 1605902.
- [56] G. Meng, Q. Yang, X. Wu, P. Wan, Y. Li, X. Lei, X. Sun, J. Liu, Hierarchical mesoporous NiO nanoarrays with ultrahigh capacitance for aqueous hybrid supercapacitor, *Nano energy*, 30 (2016) 831-839.
- [57] A. Eftekhari, The mechanism of ultrafast supercapacitors, *J. Mater. Chem. A*, 6 (2018) 2866-2876.

- [58] X. Zhang, J. Luo, P. Tang, X. Ye, X. Peng, H. Tang, S.-G. Sun, J. Fransaer, A universal strategy for metal oxide anchored and binder-free carbon matrix electrode: a supercapacitor case with superior rate performance and high mass loading, *Nano Energy*, 31 (2017) 311-321.
- [59] S. Kandula, K.R. Shrestha, N.H. Kim, J.H. Lee, Fabrication of a 3D Hierarchical Sandwich  $\text{Co}_9\text{S}_8/\alpha\text{-MnS@N-C@MoS}_2$  Nanowire Architectures as Advanced Electrode Material for High Performance Hybrid Supercapacitors, *Small*, 14 (2018) 1800291.
- [60] Y.-S. Lee, K.-S. Ryu, Study of the lithium diffusion properties and high rate performance of  $\text{TiNb}_6\text{O}_{17}$  as an anode in lithium secondary battery, *Sci. Rep.*, 7 (2017) 16617.
- [61] X. Lou, C. Lin, Q. Luo, J. Zhao, B. Wang, J. Li, Q. Shao, X. Guo, N. Wang, Z. Guo, Crystal Structure Modification Enhanced  $\text{FeNb}_{11}\text{O}_{29}$  Anodes for Lithium- Ion Batteries, *ChemElectroChem.*, 4 (2017) 3171-3180.
- [62] Y. Liu, Z. Wang, Y. Zhong, M. Tade, W. Zhou, Z. Shao, Molecular Design of Mesoporous  $\text{NiCo}_2\text{O}_4$  and  $\text{NiCo}_2\text{S}_4$  with Sub- Micrometer- Polyhedron Architectures for Efficient Pseudocapacitive Energy Storage, *Adv. Funct. Mater.*, 27 (2017) 1701229.
- [63] S. Liu, D. Ni, H.-F. Li, K.N. Hui, C.-Y. Ouyang, S.C. Jun, Effect of cation substitution on the pseudocapacitive performance of spinel cobaltite  $\text{MCo}_2\text{O}_4$  (M= Mn, Ni, Cu, and Co), *J. Mater. Chem. A*, 6 (2018) 10674-10685.
- [64] S. Baskar, D. Meyrick, K.S. Ramakrishnan, M. Minakshi, Facile and large scale combustion synthesis of  $\alpha\text{-CoMoO}_4$ : Mimics the redox behavior of a battery in aqueous hybrid device, *Chem Eng J.*, 253 (2014) 502-507.
- [65] J. Wang, X. Zhang, Q. Wei, H. Lv, Y. Tian, Z. Tong, X. Liu, J. Hao, H. Qu, J. Zhao, 3D self-supported nanopine forest-like  $\text{Co}_3\text{O}_4@\text{CoMoO}_4$  core-shell architectures for high-energy solid state supercapacitors, *Nano Energy*, 19 (2016) 222-233.

- [66] M.C. Liu, L.B. Kong, C. Lu, X.J. Ma, X.M. Li, Y.C. Luo, L. Kang, Design and synthesis of  $\text{CoMoO}_4\text{-NiMoO}_4\cdot x\text{H}_2\text{O}$  bundles with improved electrochemical properties for supercapacitors, *J. Mater. Chem. A*, 1 (2013) 1380-1387.
- [67] Z. Yin, Y. Chen, Y. Zhao, C. Li, C. Zhu, X. Zhang, Hierarchical nanosheet-based  $\text{CoMoO}_4\text{-NiMoO}_4$  nanotubes for applications in asymmetric supercapacitors and the oxygen evolution reaction, *J. Mater. Chem. A*, 3 (2015) 22750-22758.
- [68] Z. Zhang, H. Zhang, X. Zhang, D. Yu, Y. Ji, Q. Sun, Y. Wang, X. Liu, Facile synthesis of hierarchical  $\text{CoMoO}_4\text{@NiMoO}_4$  core-shell nanosheet arrays on nickel foam as an advanced electrode for asymmetric supercapacitors, *J. Mater. Chem. A*, 4 (2016) 18578-18584.
- [69] H. Liang, C. Xia, Q. Jiang, A.N. Gandi, U. Schwingenschlöggl, H.N. Alshareef, Low temperature synthesis of ternary metal phosphides using plasma for asymmetric supercapacitors, *Nano Energy*, 35 (2017) 331-340.
- [70] S. Surendran, S. Shanmugapriya, A. Sivanantham, S. Shanmugam, R. Kalai Selvan, Electrospun Carbon Nanofibers Encapsulated with NiCoP: A Multifunctional Electrode for Supercapattery and Oxygen Reduction, Oxygen Evolution, and Hydrogen Evolution Reactions, *Adv. Energy Mater.*, 8 (2018) 1800555.
- [71] G. Kresse, J. Furthmüller, Efficient iterative schemes for ab initio total-energy calculations using a plane-wave basis set, *Phys. Rev. B*, 54 (1996) 11169.
- [72] G. Kresse, D. Joubert, From ultrasoft pseudopotentials to the projector augmented-wave method, *Phys. Rev. B*, 59 (1999) 1758.
- [73] T. Watcharatharapong, M. Minakshi Sundaram, S. Chakraborty, D. Li, G. Shafiullah, R.D. Aughterson, R. Ahuja, Effect of transition metal cations on stability enhancement for molybdate-based hybrid supercapacitor, *ACS Appl. Mater. Interfaces*, 9 (2017) 17977-17991.
- [74] S. Dudarev, G. Botton, S. Savrasov, C. Humphreys, A. Sutton, Electron-energy-loss spectra and the structural stability of nickel oxide: An LSDA+ U study, *Phys. Rev. B*, 57 (1998) 1505.

[75] H.J. Monkhorst, J.D. Pack, Special points for Brillouin-zone integrations, Phys. Rev. B, 13 (1976) 5188.

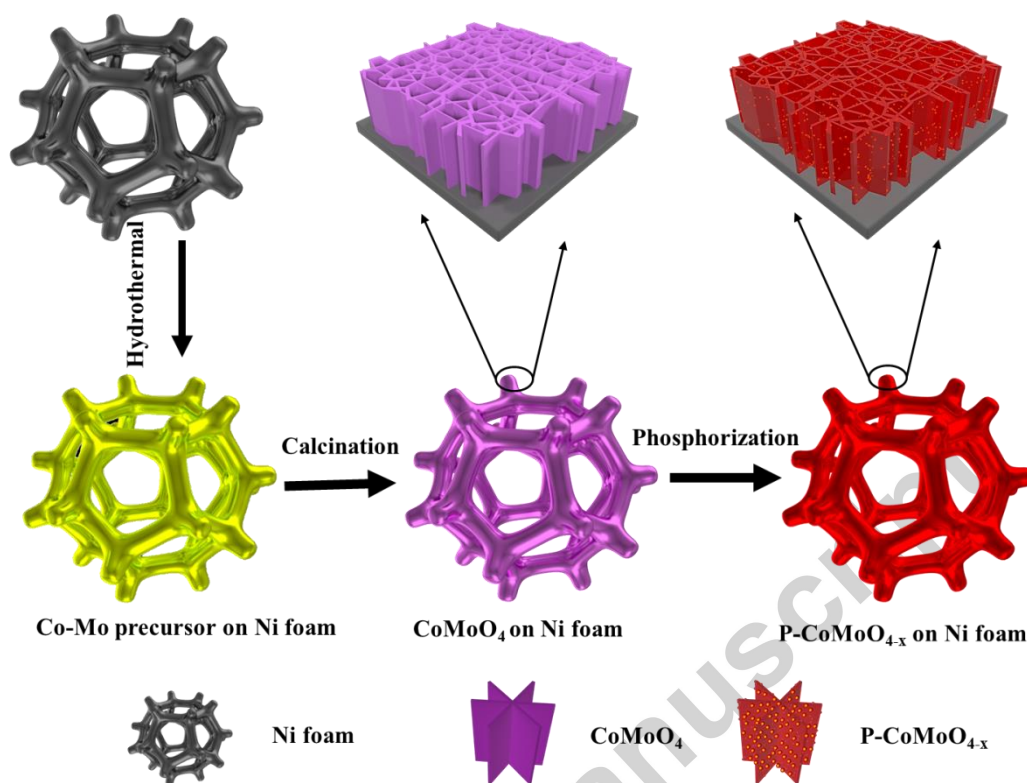


**Fig. 1.** (a) Schematic of the three-step strategy in preparing P-CoMoO<sub>4-x</sub> nanosheets.

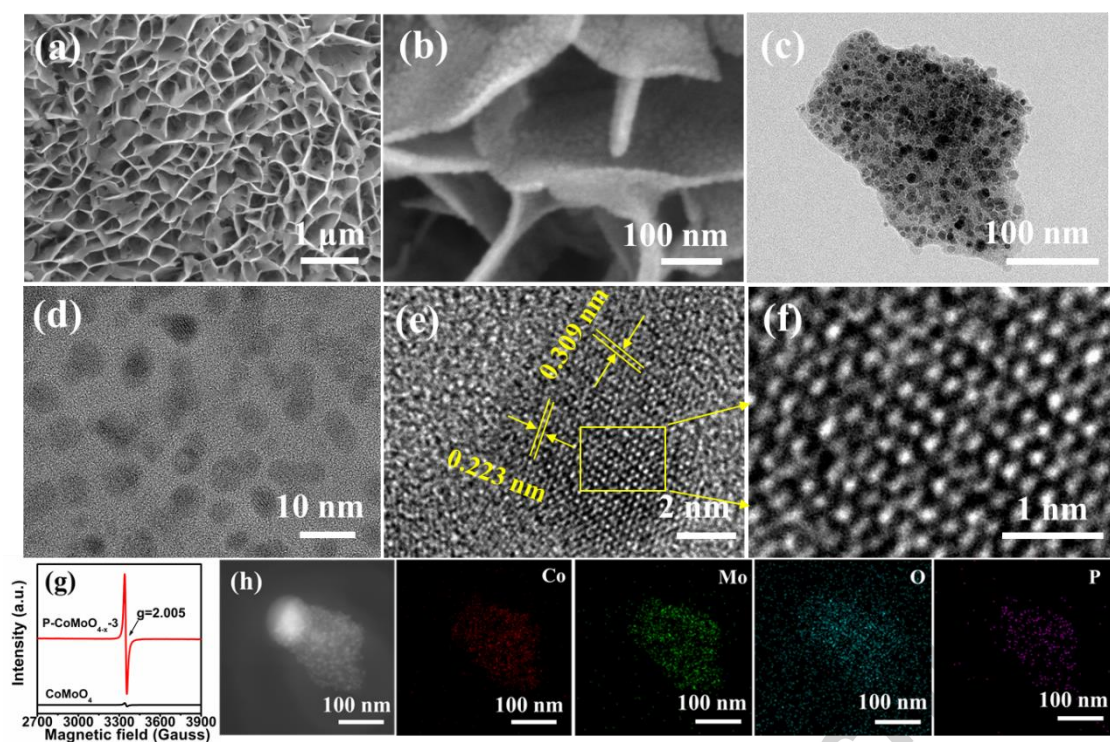


**Fig. 2.** (a, b) FESEM images, (c, d) TEM images, and (e, f) HRTEM images of P-CoMoO<sub>4-x-3</sub>. (g) EPR spectra of CoMoO<sub>4</sub> and P-CoMoO<sub>4-x-3</sub> measured at room temperature. (h) STEM-EDS mapping images of Co, Mo, O, and P recorded from a single nanosheet of P-CoMoO<sub>4-x-3</sub>.

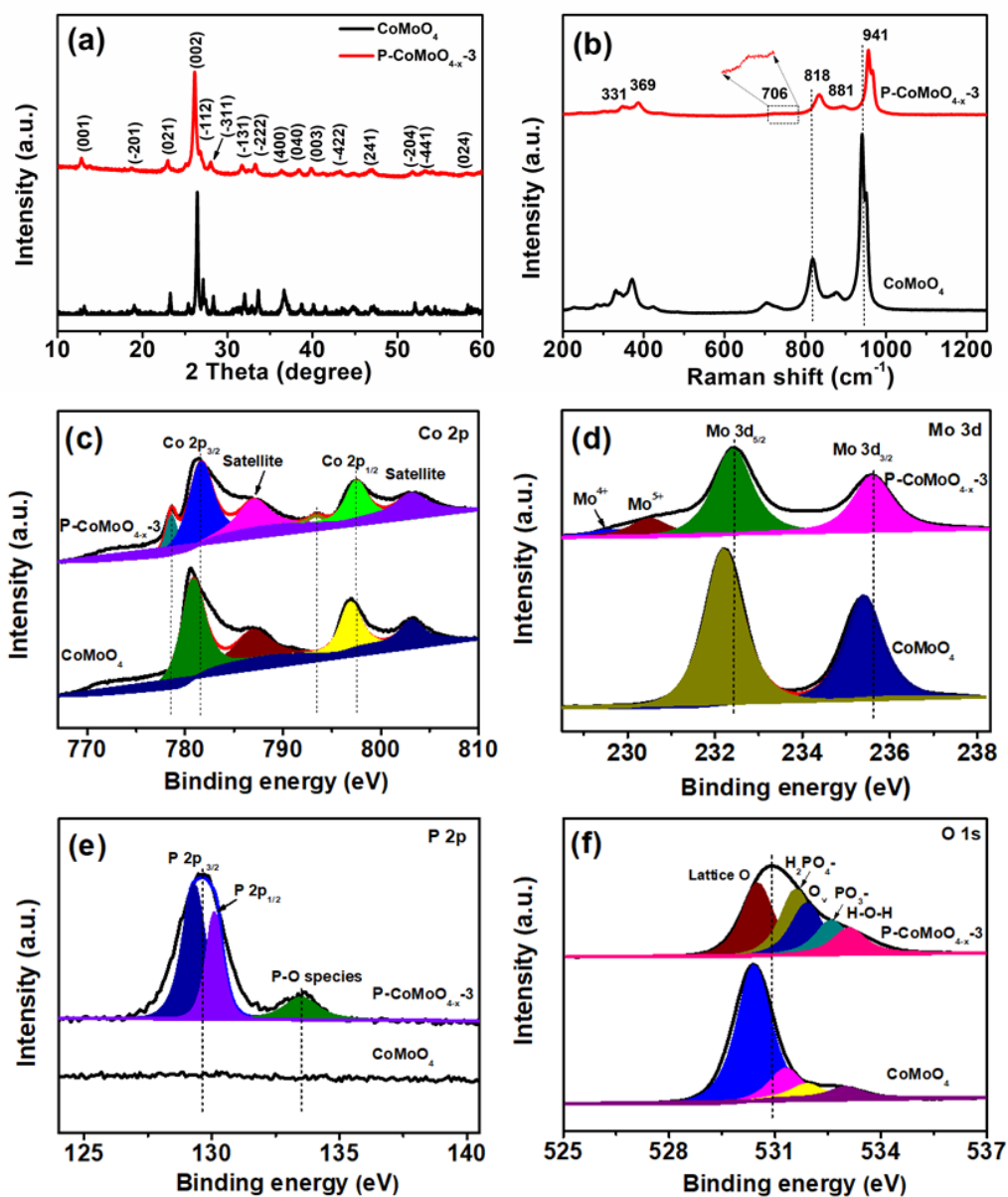


**Fig. 3.** Composition and chemical analyses of  $\text{CoMoO}_4$  and  $\text{P-CoMoO}_{4-x-3}$ : (a) XRD patterns, (b) Raman spectra, and high-resolution XPS spectra of (c) Co 2p, (d) Mo 3d, (e) P 2p, and (f) O 1s.

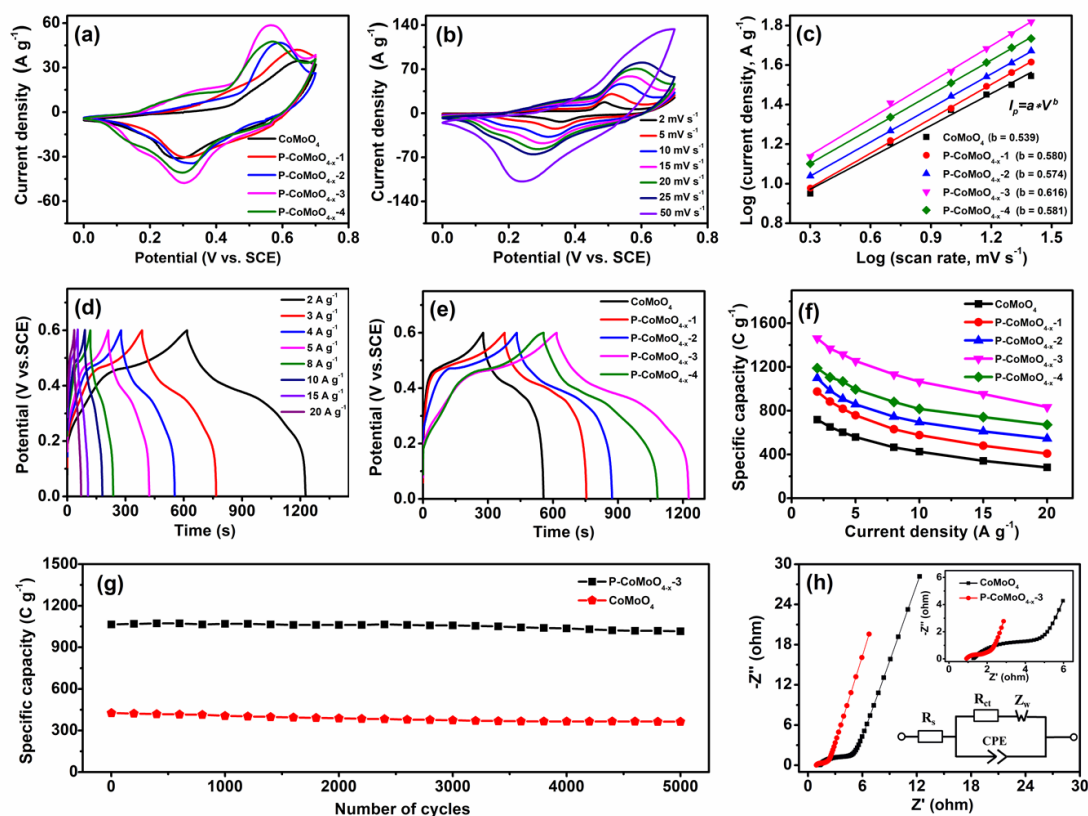


**Fig. 4.** Electrochemical performances of CoMoO<sub>4</sub> and P-CoMoO<sub>4-x-n</sub> ( $n = 1, 2, 3,$  and 4) electrodes in a standard three-electrode system. (a) Comparative CV curves of CoMoO<sub>4</sub> and P-CoMoO<sub>4-x</sub> electrodes obtained at a scan rate of 15 mV s<sup>-1</sup>. (b) CV curves of P-CoMoO<sub>4-x-3</sub> electrode obtained at different scan rates. (c) Power law dependence of redox peak current on scan rate for CoMoO<sub>4</sub> and P-CoMoO<sub>4-x</sub> electrodes. (d) GCD curves of P-CoMoO<sub>4-x-3</sub> electrode obtained at different current densities. (e) Comparative GCD curves of CoMoO<sub>4</sub> and P-CoMoO<sub>4-x</sub> electrodes obtained at a current density of 2 A g<sup>-1</sup>. (f) Specific capacities of CoMoO<sub>4</sub> and P-CoMoO<sub>4-x</sub> electrodes as function of current density. (g) Cycling stability of CoMoO<sub>4</sub> and P-CoMoO<sub>4-x-3</sub> electrodes at a current density of 10 A g<sup>-1</sup>. (h) Nyquist plots with insets showing the magnified semicircles and electrochemical equivalent circuits of CoMoO<sub>4</sub> and P-CoMoO<sub>4-x-3</sub> electrodes.

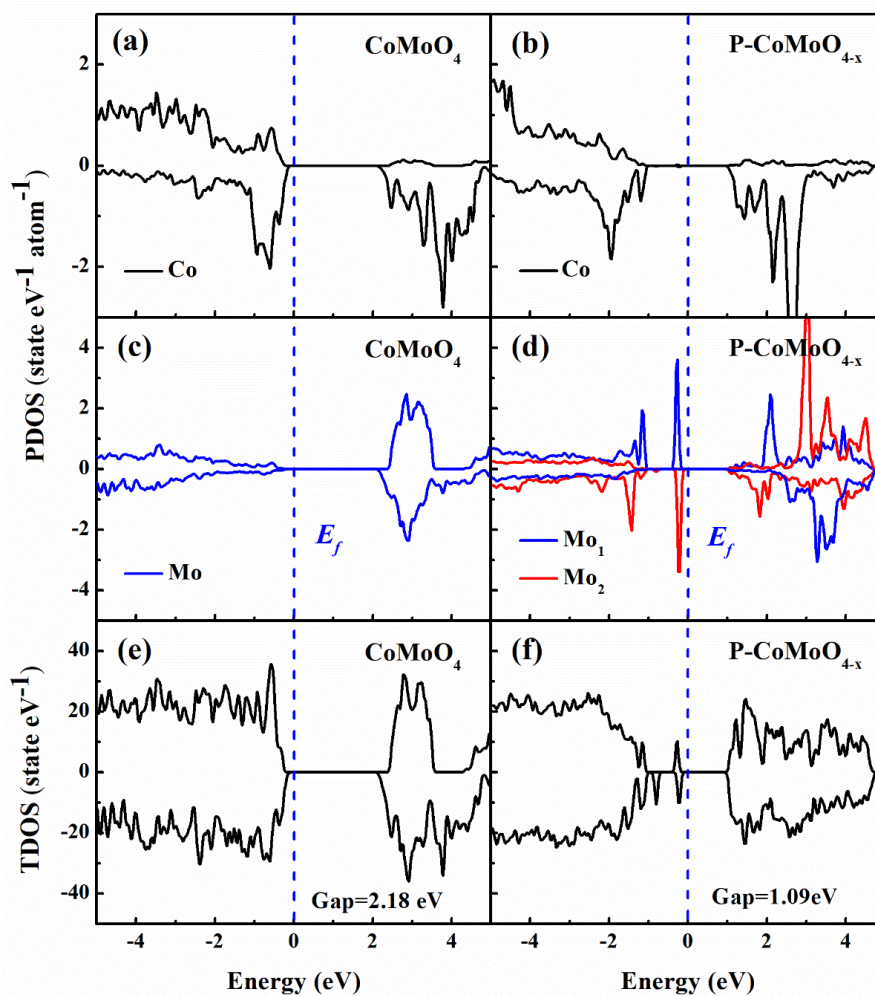


**Fig. 5.** Projected DOS (PDOS) of the Co-3d states of Co atoms in  $\text{CoMoO}_4$  (a) and  $\text{P-CoMoO}_{4-x}$  (b). PDOS of Mo-4d states for Mo atoms in  $\text{CoMoO}_4$  (c) and  $\text{P-CoMoO}_{4-x}$  (d). Total DOS of  $\text{CoMoO}_4$  (e) and  $\text{P-CoMoO}_{4-x}$  (f). Fermi level is set to 0 eV.

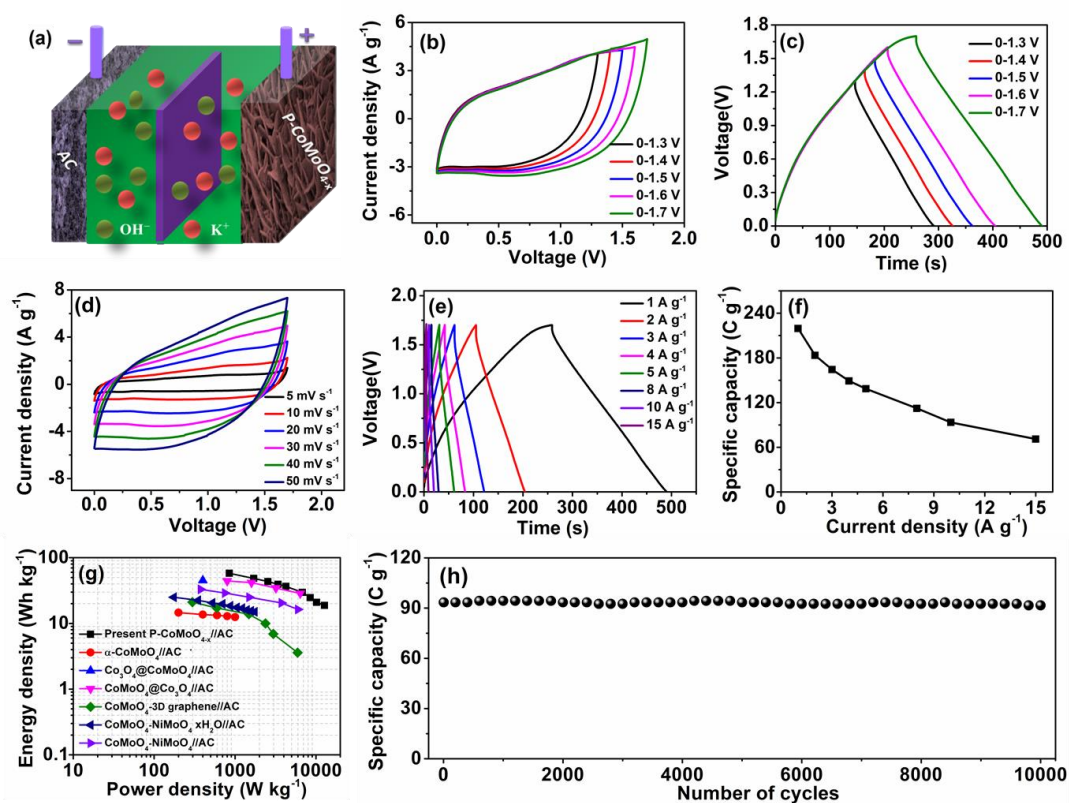


**Fig. 6.** Electrochemical characterization of the assembled P-CoMoO<sub>4-x</sub>//AC device: (a) Schematic of device fabrication; (b) CV curves collected at various voltage windows at 30 mV s<sup>-1</sup>; (c) GCD curves collected at various voltage windows at 1 A g<sup>-1</sup>; (d) CV curves obtained at different scan rates; (e) GCD curves obtained at various current densities; (f) specific capacity as a function of various current densities; (g) comparison of the Ragone plots of the present and reported devices; and (h) cycling stability at a current density of 10 A g<sup>-1</sup>.